Ultrathin Amorphous Silica Membrane Enhances Proton Transfer across Solid-to-Solid Interfaces of Stacked Metal Oxide Nanolayers While Blocking Oxygen

*Won Jun Jo, Georgios Katsoukis, and Heinz Frei**

Dr. W. J. Jo, Dr. G. Katsoukis, Dr. H. Frei

Molecular Biophysics and Integrated Bioimaging Division, Lawrence Berkeley National Laboratory, University of California, Berkeley, CA 94720, USA

E-mail: HMFrei@lbl.gov

(*Adv. Funct. Mater.*, in press)

Keywords:

Ultrathin silica layer, proton transfer, stacked metal oxide nanolayers, solid-solid interfaces, nanoscale integration, incompatible catalysis environments

Abstract

A large jump of proton transfer rates across solid-to-solid interfaces by inserting an ultrathin amorphous silica layer into stacked metal oxide nanolayers is discovered using electrochemical impedance spectroscopy and FT-IRRAS. The triple stacked nanolayers of Co_3O_4, SiO_2, and TiO_2 prepared by atomic layer deposition (ALD) enable a proton flux of 2,400 $\pm$ 60 s^{-1} nm^{-2} (pH 4, room temperature), while a single TiO_2 (5 nm) layer exhibits a 3-fold lower flux of 830 s^{-1} nm^{-2}. Based on FT-IRRAS measurements, this remarkable enhancement is proposed to originate from the sandwiched silica layer forming interfacial SiOTi and SiOCo linkages to TiO_2 and Co_3O_4 nanolayers, respectively, with the O bridges providing fast H^+ hopping pathways across the solid-to-solid interfaces. Together with the complete O_2 impermeability of a 2 nm ALD-grown SiO_2 layer, the high flux for proton transport across multi-stack metal oxide layers opens up the integration of incompatible catalytic environments to form functional nanoscale assemblies such as artificial photosystems for CO_2 reduction by H_2O.

1. Introduction

The emergence of ultrathin oxide layers has recently led to breakthroughs in catalysis for energy, notably the efficiency and durability of catalytic components, more facile methods for combining catalysts with electron sources and light absorbers, or coupling incompatible reaction environments that enables systems integration on the nanoscale. Prominent examples among these are nanoscale titania protection layers of semiconductor photoanodes for water oxidation that dramatically increase their stability, [1-4] opening up the utilization of corrosion-prone III-V semiconductor materials thereby enabling the development of high efficiency solar water splitters.[3,4] Chromia, silica, or nickel oxide nanolayers for encapsulating noble metal catalyst particles were introduced for enhancing the efficiency of hydrogen evolution by blocking O_2 and undesirable metal ion access to the catalyst surface, suppressing back reaction and catalyst poisoning.[5-9] The proton and hydrogen atom permeability of silica nanolayers was exploited for electroreduction at metal catalysts separated from n-Si electrode by an ultrathin SiO_2 protection layer[10] (orders of magnitude thicker silica films, or amorphous silica-based double oxides, are used as H^+ conducting membranes in intermediate temperature fuel cells).[11,12] Ultrathin transition metal oxide co-catalyst layers such as Co oxide on semiconductor photoelectrodes improved charge transfer between light absorber and catalyst as well as water oxidation activity.[13] For systems using molecular components anchored on electrode surfaces, embedding in ultrathin alumina or titania layers led to remarkable improvement of the durability of surface attachment of the organic components while facilitating the coupling among them by obviating the need for molecularly defined linkages.[14,15]

Ultrathin oxide layers enable us to address the challenge of nanoscale integration of incompatible catalytic environments such as those of water oxidation and carbon dioxide

reduction for the first time through their separation by a membrane on this shortest possible length scale while maintaining their electronic and protonic communication. To this end, we have recently introduced ultrathin silica layers with embedded molecular wires as gas impermeable, charge and proton conducting membranes.[16,17] Controlled charge transport across ultrathin insulating silica membranes was achieved by embedded molecular wires (*p*-oligo(phenylene vinylene)), which were characterized by short circuit photoelectrochemical and ultrafast optical measurements.[18-23] Such a functional silica nanomembrane separating incompatible inorganic and microbial environments was demonstrated.[18]

Proton transport and gas permeability properties based on cyclic voltammetry (CV) measurements have recently been reported for single oxide nanolayers such as ultrathin silica prepared by atomic layer deposition[18,24] or ozone treatment of spin-cast Si precursor,[7] or for chromia nanolayers prepared by solution-based photo- or electrodeposition methods.[25] However, the development of functional nanoscale systems typically requires integration of ultrathin structures with higher degree of complexity. For example, nanoscale artificial photosynthetic systems require incorporation of catalytic function and chemical separation. This poses the challenge of delivering charges and protons across multiple adjoined layers and associated interfaces while at the same time preventing undesired crossover of chemical species. Here, we investigate H^+ conductivity and O_2 impermeability of multi-oxide stacked nanolayers and find that ultrathin silica membranes introduce interfacial properties which enhance proton transport while enabling complete blocking of oxygen. The corresponding proton and oxygen transport properties of the multi-oxide nanolayers were analyzed by the complementary implementation of Fourier-transform infrared reflection absorption spectroscopy (FT-IRRAS), CV, and electrochemical impedance spectroscopy (EIS). For the purpose of artificial

photosystems, they exceeded the requirements for fully harnessing maximum solar-photon flux under any systems geometry.

2. Results

Using a planar Pt film (100 nm) on Si wafer support as electrode and as reflective surface for infrared probing, Pt-H absorbance growth via H under-potential deposition ($H^+ + Pt \rightarrow Pt\text{-}H$, commonly referred to as H_{upd})[7] was observed by FT-IRRAS. H^+ flux through single SiO_2, Co_3O_4, and TiO_2 nanolayers, and multiple stacked layers (cartoon Figure S1) was quantitatively monitored by EIS, while O_2 permeation behavior was characterized by cyclic voltammetry (CV).

2.1. Structural Characterization of Oxide Nanolayers and Interfaces by FT-IRRAS

The FT-IRRAS method provides the most detailed structural characterization of planar nanoscale oxide layers and interfaces because of its high surface sensitivity due to the electric field enhancement of perpendicularly polarized infrared modes, the ability to monitor signals from

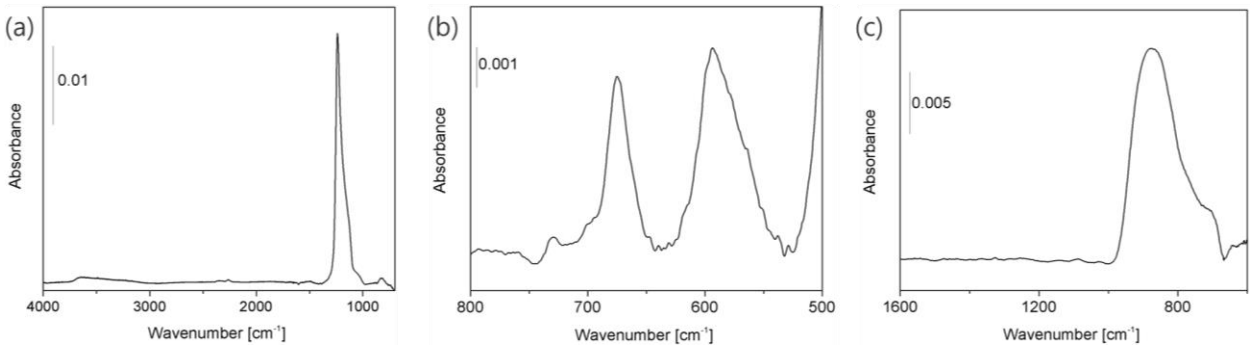

Figure 1. IRRAS of **(a)** SiO_2 (2 nm). **(b)** Co_3O_4 (3.5 nm). **(c)** TiO_2 (10 nm). The spectra are baseline corrected with a polynomial function.

amorphous and crystalline phases alike, and to probe interfacial chemical bonds. The p-polarized FT-IRRAS of 2 nm SiO_2 samples reveals a characteristic, intense absorption of the longitudinal optic (LO) asymmetric SiOSi stretch mode at 1236 cm^{-1} with a shoulder at 1150 cm^{-1} (in- and out-of-phase motion of two adjacent O atoms with respect to the center Si atom)[26-30] shown in **Figure 1(a)**. Interestingly, the corresponding transverse optic (TO) asymmetric ν(SiOSi) mode of amorphous silica wafers with a sharp peak at 1080 cm^{-1} is not observed because this mode cannot absorb p-polarized light.[31] Aside from the symmetric SiOSi mode at 820 cm^{-1} and an extremely weak band of the OH stretch mode of isolated SiOH groups at 3747 cm^{-1} that was observed for some samples, no other infrared bands are detected in the region 4000 – 600 cm^{-1}, which confirms that the SiO_2 layers are free of organic impurities. Specifically, no bands of CH stretch modes in the 3000-2800 cm^{-1} region, characteristic of $N(CH_3)_2$ fragments of incompletely converted 3DMAS precursor molecules, were detected.[28] Importantly, we found a linear relationship between the 1236 cm^{-1} LO SiOSi band intensity and the ALD layer thickness as measured by the number of ALD cycles. Comparison with thicknesses measured for the same samples by ellipsometry allowed us to assign silica layer thickness based on the observed 1236 cm^{-1} absorption intensity.

The FT-IRRAS of a 3.5 nm ALD grown of Co oxide layers reveals CoO stretch absorption peaks at 675 and 592 cm^{-1}, shown in **Figure 1(b)**. These bands, including relative intensity, are characteristic of ultrathin layers of Co_3O_4 (spinel) structure[32] and readily distinguished from other Co oxide structures, specifically CoO,[32,33] Co(O)OH,[33] and Co_2O_3.[34] In particular, the single sharp bands of the latter three structures in the region 510 to 590 cm^{-1} are not observed. We conclude that Co_3O_4 is the dominant phase of the ultrathin Co oxide film prepared by ALD. In contrast to conformal SiO_2 layers, ALD-grown Co_3O_4, while uniform, is

known to possess nanogranular morphology[22,35] composed of 3-5 nm diameter crystals as manifested by AFM and STEM-EDX (Co) analysis reported of the previous work.[22]

As **Figure 1(c)** displays, the 10 nm TiO_2 ALD layer features a broad band with maximum at 870 cm^{-1} assigned to the TiOTi LO mode of anatase structure.[36-38]

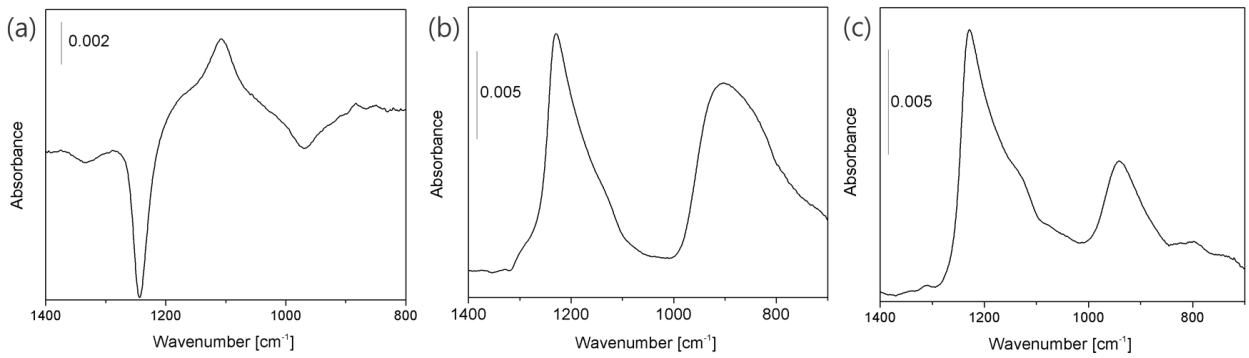

Figure 2. (a) IRRAS difference spectrum of Co_3O_4 (3.5 nm)/SiO_2 (2 nm) from which the Pt/SiO_2 (2 nm) trace was subtracted. The negative band at 1247 cm^{-1} is due to a red shift and enhanced intensity of the LO SiOSi mode for SiO_2 interacting with the Pt substrate. **(b)** IRRAS of TiO_2 (10 nm)/SiO_2 (2 nm)/Co_3O_4 (3.5 nm). The spectrum was baseline corrected with a polynomial function. **(c)** IRRAS difference spectrum of TiO_2 (10 nm)/SiO_2 (2 nm)/Co_3O_4 (3.5 nm) from which the TiO_2 trace (Figure 1(c)) and Co_3O_4 trace (Figure 1(b)) were subtracted.

For Co_3O_4 (3.5 nm)/SiO_2 (2 nm) and TiO_2 (10 nm)/SiO_2 (2 nm)/Co_3O_4 (3.5 nm) multilayer samples on Pt, Figure 2 shows new infrared absorption bands in addition to those observed for pure SiO_2, Co_3O_4 and TiO_2 ALD layers of Figure 1, indicating the formation of interfacial SiOCo and SiOTi linkages. For Co_3O_4 (3.5 nm)/SiO_2 (2 nm), **Figure 2(a)** shows the difference obtained by subtraction of the spectrum of bare SiO_2 (2 nm), revealing a band at 1110 cm^{-1}. This absorption, which overlaps with the intense SiO_2 asymmetric stretch mode, is attributed to the interfacial ν(Si-O-Co) bond mode based on the close agreement with Si-O-Co stretch modes of a silane molecule anchored on Co_3O_4 nanolayer.[39] For TiO_2 (10 nm)/SiO_2 (2 nm)/Co_3O_4 (3.5 nm), an absorption is observed 940 cm^{-1} (**Figure 2(b)**) that is not present in the

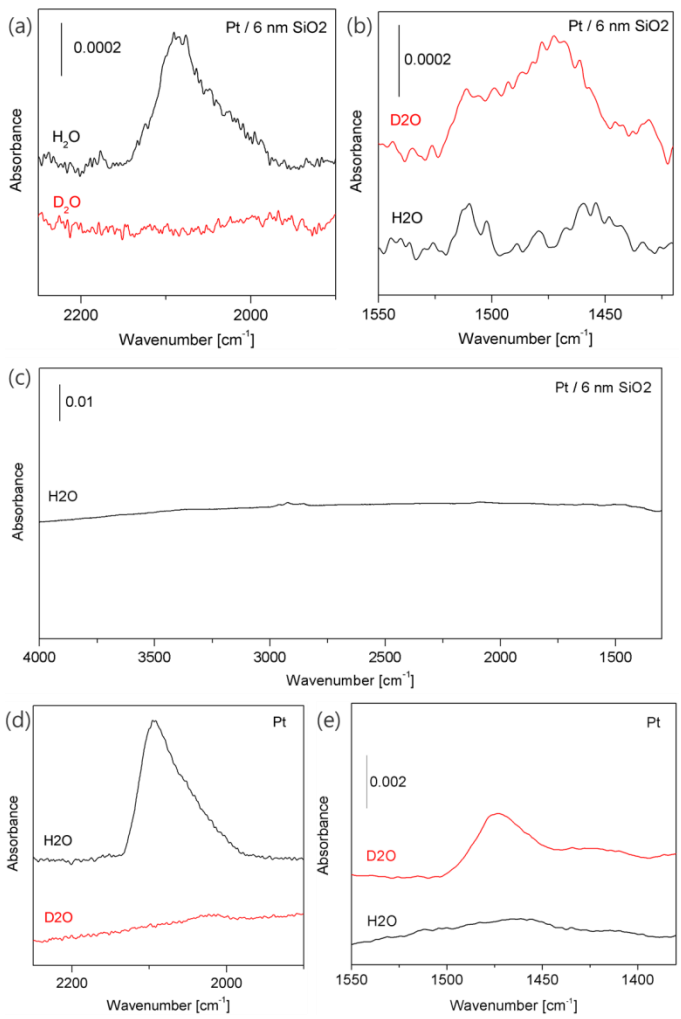

Figure 3: FT-IRRAS of Pt-H and Pt-D growth observed following H_{upd} in pH 4 (pD 4) aqueous electrolytes. **(a)** Top trace: Growth of Pt-H mode recorded after CV sweeps of Pt/SiO_2 (6 nm) electrode in H_2O in the range 1.2-0.02 V vs. RHE. Bottom trace: Same experiment in D_2O. **(b)** Top trace: Growth of Pt-D mode after CV sweeps of Pt/SiO2 (6 nm) electrode in D_2O. Bottom trace: Same experiments in H_2O. **(c)** Survey spectrum after CV sweeps of Pt/SiO_2 (6 nm) in H_2O. **(d)** Top trace: Growth of Pt-H mode recorded after CV sweeps of bare Pt electrode in H_2O in the range1.2-0.02 V vs. RHE. Bottom trace: Same experiment in D_2O. **(e)** Top trace: Growth of Pt-D mode after CV sweeps of bare Pt electrode in D_2O. Bottom trace: Same experiments in H_2O.

spectrum of bare TiO_2. The new band, assigned to the Si-O-Ti stretch mode,[36,40] overlaps with ν(TiOTi) of the TiO_2 layer at 870 cm^{-1} and is therefore more clearly seen when subtracting the TiO_2 trace (**Figure 1(c)**) from the spectrum of **Figure 2(b)**, as **Figure 2(c)** displays. While stretch modes of SiOH groups absorb also around 950 cm^{-1}, any significant contribution from

these modes is ruled out because no SiOH stretch absorption was noted for this sample. Hence, we conclude that the stacked ALD layers of Co_3O_4, SiO_2, and TiO_2 form readily observed covalent bonds across the interfaces.

2.2 Monitoring Proton Flux across SiO_2 Nanolayers via H Underpotential Deposition by FT-IRRAS and EIS, and O_2 Impermeability by CV

As the top traces of **Figures 3(a)** and **3(b)** show, p-polarized FT-IRRAS allowed us to detect the growth of Pt-H (Pt-D) infrared modes upon H (D) under-potential deposition (CV sweeps 1.2 – 0.02 V vs. RHE), initiating proton transfer across the electrolyte/SiO_2 interface of Pt/SiO_2 (6 nm) electrodes exposed to pH 4 (pD 4) electrolyte. The spectroscopic assignment was confirmed by the absence of the corresponding bands in experiments with the alternate isotopic modification (the bottom traces of Figure 3(a) and 3(b)), also consistent with literature.[41,42] Underpotential deposition was conducted using the Pt/SiO_2 (6 nm) sample as a working electrode in the standard three-electrode cell configuration containing N_2 purged aqueous electrolyte at pH 4 (pD 4). Exposure of the Pt/SiO_2 sample to oxygen was prevented during H_{upd} (verified by the absence of an oxygen reduction wave), followed by Ar flow drying and air-tight transfer to N_2-purged FT-IR spectrometer sample compartment. As the IRRAS overview spectrum in **Figure 3(c)** shows, characteristic H_2O bands at 1635 and 3500 cm^{-1} are completely absent, indicating that no water molecules are trapped at the Pt/SiO_2 interface, and no hydration of the amorphous SiO_2 film occurs during H_{upd}. Therefore, the growth of the Pt-H (Pt-D) band by H (D) underpotential deposition originates from the reduction of protons transported from the pH 4 (pD 4) aqueous phase through the conformal amorphous SiO_2 nanolayer to the Pt surface, rather than from the

reduction of trapped H_2O (D_2O) molecules. No loss of SiO_2 absorption at 1236 cm^{-1} was noted after multiple underpotential deposition runs, confirming the stability of the ultrathin ALD layer.

FT-IRRAS results of identical $H(D)_{upd}$ experiments using bare Pt, shown in **Figures 3(d)** and **3(e)**, respectively, gave the same Pt-H and Pt-D bands as the Pt/SiO_2 samples. The distinct difference between H_{upd} using bare Pt and ultrathin SiO_2 covered Pt is that water molecule reduction instead of H^+ reduction predominantly occurs at bare Pt electrodes in pH 4 solution,[43] while protons are exclusively reduced at the Pt/SiO_2 interface.

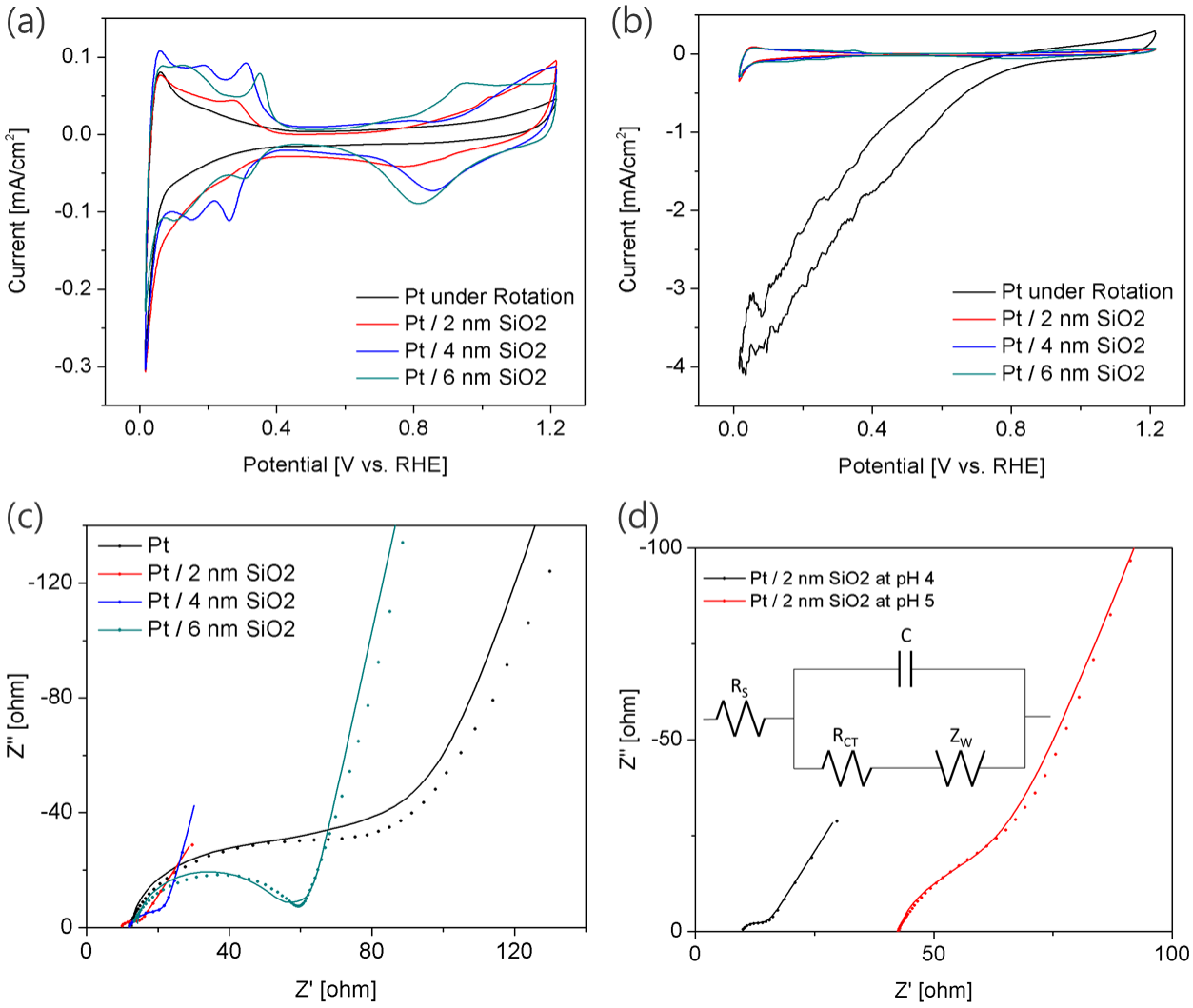

Figure 4. (a) CV of bare Pt electrode (black trace) and Pt covered by 2, 4, and 6 nm SiO_2 (red, blue, and green traces) at 298 K in N_2 saturated aqueous 0.5 M Na_2SO_4 solution at pH 4, adjusted by H_2SO_4. Scan rate 50 mV s^{-1}. **(b)** CV in O_2 bubbled electrolyte solution under the same conditions. **(c)** EIS in N_2 saturated electrolyte pH 4 solution used for (a). Applied potential was 0.096 vs. RHE. The dots in the plot are the experimental data and the solid lines represent the results of fitting the data to the equivalent circuit (Randles circuit) shown in the inset of (d). For all CV data, the solution correction was applied and its effect found negligible. **(d)** EIS of Pt/SiO_2 (2 nm) electrode in N_2 saturated aqueous solution at pH 5 and pH 4, applied potential 0.096 vs. RHE.

Using Pt coated with 2, 4, and 6 nm SiO_2 thickness as WE in the three-electrode cell containing N_2 purged pH 4 electrolyte, CV sweeps were conducted in the range from 1.216 to 0.016 V vs. RHE. As **Figure 4(a)** illustrates for the case of the 2 nm SiO_2 sample, the CV wave (red trace) exhibits cathodic current in the range 0.4 to 0 V due to H_{upd} at the Pt/SiO_2 interface. The curve closely resembles that of bare Pt (black trace), but exhibits somewhat larger cathodic current (CV waves for different scan rates (25, 50, 100 mV s^{-1}) confirmed the expected linear increase of the H_{upd} current with increasing scan rate).[44] It should be noted that the typical sharp H_{upd} peaks observed for CV curves are absent for bare Pt and the 2 nm silica samples, but pronounced for 4 nm and 6 nm silica coating. While this phenomenon was reported by others,[7] including the absence for bare Pt contrasting with distinct peaks upon deposition of SiO_2 nanolayers as observed in **Figure 4(a)**,[45] we identified as cause in our case here the specific preparation method of the Pt layer; CV curves of Pt samples prepared by substrate rotation during e-beam evaporation did not show peaks, while CV curves of Pt samples prepared without rotating the substrate during evaporation did exhibit distinct H deposition peaks, as shown in Figure S2. The observed substrate rotation effect most probably reflects different Pt crystal facets exposed at the surface.

CV sweeps with the same Pt/SiO_2 WEs in O_2 bubbled electrolyte solution showed only the H_{upd} signal without O_2 reduction wave compared to bare Pt (**Figure 4(b)**). The measurements reveal that the ALD-grown, pinhole-free layer (≥ 2 nm) completely blocks O_2.

Accurate proton flux measurements require the use of EIS which, as an AC method, reports the rates of ion species transport and reaction close to equilibrium.[44] EIS was carried out at a potential of 0.096 V vs. RHE appropriate for H_{upd}. **Figure 4(c**) presents Nyquist plots for 2, 4, and 6 nm SiO_2 ALD layers with the equivalent electrical circuit used for numerical data analysis. *X* and *y* axes represent the real and imaginary part (negative value) of the measured impedance, respectively. Since EIS data were measured using the three-electrode cell configuration, the arc region of the Nyquist plot represents charge transfer resistance, while the linear region represents mass transfer impedance across the SiO_2 coated Pt electrode. According to the IRRAS results, the infrared growth of Pt-H by H_{upd} originates from the reduction of protons transported from the pH 4 electrolyte through the conformal amorphous SiO_2 nanolayer to the Pt surface. Therefore, an appropriate equivalent circuit is required to quantify the influence of H^+ transport from the electrolyte to the Pt surface via the ultrathin SiO_2 layer.[44-47] We selected the generalized Randles circuit shown in **Figure 4(c)** and **Figure S3** where R_S is the solution resistance, *C* the double layer capacitance at the Pt/SiO_2 interface, R_{CT} the charge transfer resistance across the interface, and Z_W the mass transfer impedance (Warburg impedance) at the electrolyte/SiO_2 interface.[44,47,48]

Based on the equivalent circuit model, EIS data fitting was performed using ZView software.[49] As a result, Z_W of 6.8 Ω was obtained for the 2 nm SiO_2 sample. Given the applied voltage V = 1.1 V between working and counter electrode, a current $I = V/Z_W$ = 0.16 A is calculated, corresponding to a current density *J* of 0.24 A cm^{-2} (exposed surface area 0.68 cm^2)

and, hence, a H^+ flux of 15,000 s^{-1} nm^{-2}. Results including error bars for all samples examined are summarized in Table 1.

The SiO_2 thickness dependence of the measured H^+ flux follows quantitatively the expected dependence on the H^+ concentration gradient across the SiO_2 layer as predicted by Fick's law,[44] with the flux decreasing from 2 nm to 6 nm layers (**Table 1**). The good agreement with the observed H_{upd} current validates the use of the Randles equivalent circuit and of the Warburg mass transport impedance for calculating the H^+ flux. The diminishing H^+ flux with increasing SiO_2 layer thickness requires more reducing potential in order to maintain the same cathodic current; a two nm Pt/SiO_2 electrode produces -0.12 mA cm^{-2} at 0.096 V vs. RHE, while 4 and 6 nm samples reach -0.12 mA cm^{-2} at more negative potentials of 0.057 V and 0.051 V, respectively.

To further test the chosen equivalent circuit model, we determined H^+ flux also for pH 5 and pH 4 solution, with Nyquist plots presented in **Figure 4(d)** (experiments at pH below 4 are not reliable because the Ti adhesion layer between the Si wafer support and the Pt nanolayer corrodes under these conditions). For a Pt/SiO_2(2 nm) sample, Z_W increases from 6.8 Ω at pH 4 to 64 Ω at pH 5 corresponding to H^+ flux decrease by a factor of 10.7 $\pm$ 4.0 (from 15,000 to 1,400 s^{-1} nm^{-2}). The pH effect is in agreement with the proton gradient dependence according to Fick's law. The H^+ conductivity $\kappa = l/(Z_W \times A)$ (l = SiO_2 layer thickness, A = SiO_2 surface area) of 3.8 x 10^{-8} S cm^{-1} for pH 4 is in the same range as predicted for few μm thick SiO_2 films at room temperature when extrapolating from measurements at 100 °C,[50] or for SiO_2 glass measured at 40 °C.[51] These observations further validate the choice of the equivalent circuit and Z_W as impedance parameter for determining the H^+ flux.

2.3 Electrochemical Monitoring of Proton Flux and O_2 Permeation of Single Co_3O_4 and TiO_2 Nanolayers

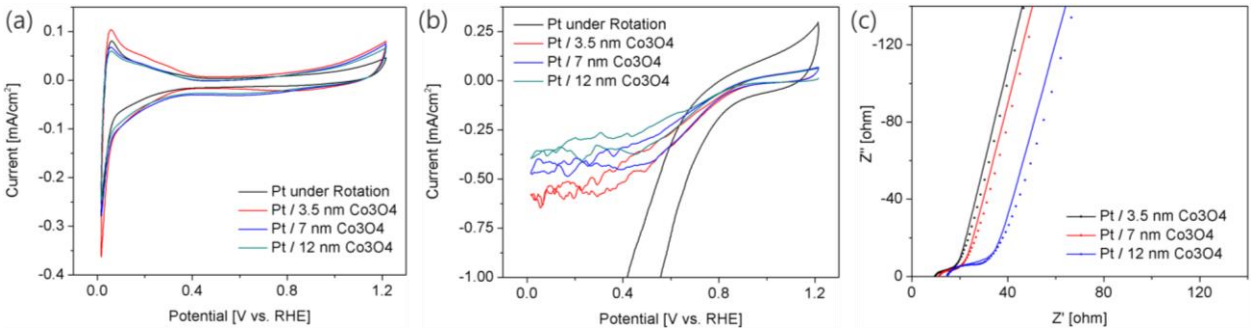

Figure 5. (a) CV of bare Pt electrode (black trace) and Pt covered by 3.5, 7, and 12 nm Co_3O_4 (red, blue, and green trace) at 298 K in N_2 saturated aqueous 0.5 M Na_2SO_4 solution at pH 4, adjusted by H_2SO_4. Scan rate 50 mV s^{-1}. **(b)** CV in O_2 bubbled electrolyte solution under the same conditions. **(c)** EIS in N_2 saturated electrolyte solution used for (a). Applied potential was 0.096 V vs. RHE. The small dots in the plot are the experimental data and the solid lines represent the results of fitting the data to the Randles circuit.

CV sweeps for Pt/Co_3O_4 (3.5, 7, and 12 nm) electrodes were conducted under the identical conditions used for Pt/SiO_2 electrodes. As **Figure 5(a)** shows, cathodic currents from 0.4 to 0.016 V in N_2 saturated electrolyte are close to those obtained for bare Pt. Oxygen reduction currents in O_2 bubbled electrolyte, while smaller than that of bare Pt, indicate substantial oxygen permeability through ALD-grown Co_3O_4 layers (**Figure 5(b)**). As expected, the current decreases monotonously with increasing layer thickness. Proton conductivity for the three Co_3O_4 layers was evaluated by EIS using the same experimental conditions and analysis approach as the SiO_2 case, with the resulting Nyquist plots shown in **Figure 5(c)**. The Z_W impedance for proton diffusion across the 12 nm Co_3O_4 layer is 37.1 Ω. With an exposed surface of 0.64 cm^2, we calculate a proton adsorption current density of 0.047 A cm^{-2}, corresponding to a H^+ flux of 2,900 s^{-1} nm^{-2}. The Co_3O_4 thickness impact on the H^+ flux summarized in Table 1 is consistent

with the proton gradient dependence predicted by Fick's law. The H^+ conductivity of Co_3O_4 nanolayers derived from the values presented in Table 1 is 5.2 x 10^{-8} S cm^{-1}.

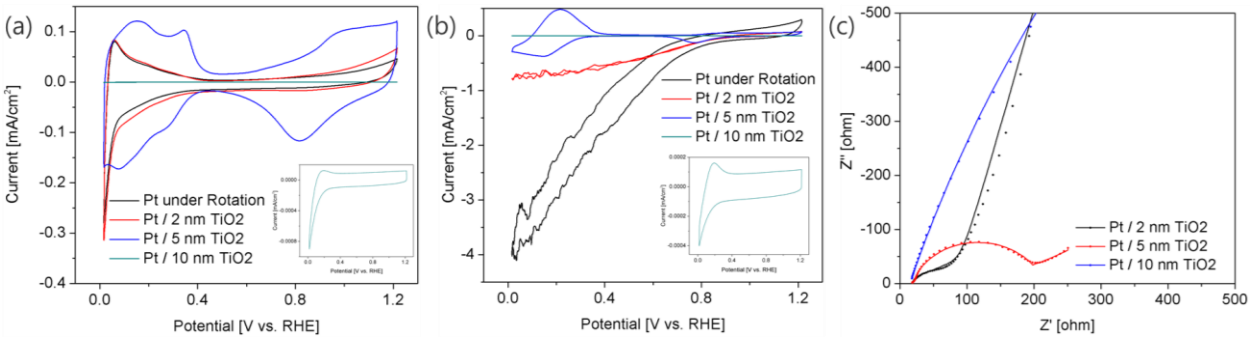

Figure 6. (a) CV of bare Pt electrode (black traces) and Pt covered by 2, 5, and 10 nm TiO_2 (red, blue, and green traces with magnified view for 10 nm sample in the inset) at 298 K in N_2 saturated aqueous 0.5 M Na_2SO_4 solution at pH 4, adjusted by H_2SO_4. Scan rate 50 mV s^{-1}. **(b)** CV in O_2 bubbled electrolyte solution under the same conditions. Inset: Magnified view for 10 nm sample. **(c)** EIS in N_2 saturated electrolyte solution used for (a). Applied potential was 0.096 V vs. RHE. The small dots in the plot are the experimental data and the solid lines represent the results of fitting the data to the Randles circuit.

Ultrathin titania layers exhibit proton conductivity but at much lower rates. **Figure 6(a)** and **6(b)** present CV sweeps for Pt/TiO_2 (2,5, and 10 nm) electrodes in N_2 saturated and O_2 bubbled electrolyte solutions, respectively. Here, it should be noted that TiO_2 layers thicker than 5 nm also block O_2 diffusion like SiO_2 layers. The quantitative determination of proton flux through 5 nm thick TiO_2 layer by EIS gave Z_W of 305.3 Ω. With an electrode surface of 0.27 cm^2, a proton adsorption current is estimated to be 0.013 A cm^{-2}, corresponding to a proton flux 830 s^{-1} nm^{-2} and conductivity of 6.1 x 10^{-9} S cm^{-1}. This low value points to inefficient H^+ transfer across the TiO_2/electrolyte interface and/or inferior H^+ hopping through TiO_2 nanolayer (the latter being ruled out in the following).

2.4 Electrochemical Characterization of Proton Flux and O_2 Impermeability of Multi-Oxide Stacked Nanolayers

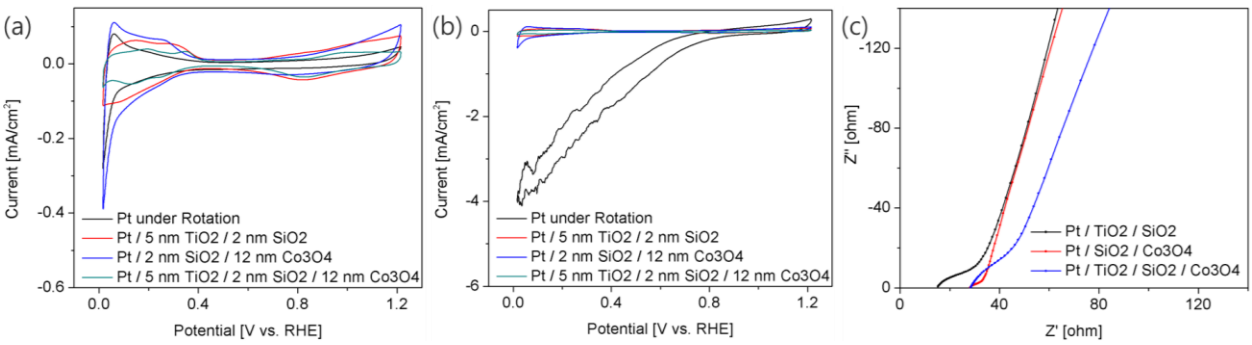

Figure 7. (a) CV of bare Pt electrode (black trace), Pt covered by TiO_2 (5 nm)/SiO_2 (2 nm) (red trace), SiO_2 (2nm)/Co_3O_4 (12 nm) (blue trace) and TiO_2 (5 nm)/SiO_2 (2 nm)/Co_3O_4 (12 nm) (green trace) at 298 K in N_2 saturated aqueous 0.5 M Na_2SO_4 solution at pH 4, adjusted by H_2SO_4. Scan rate 50 mV s^{-1}. **(b)** CV in O_2 bubbled electrolyte solution under the same conditions. **(c)** EIS in N_2 saturated electrolyte solution used for TiO_2 (5 nm)/SiO_2 (2 nm) (black trace), SiO_2 (2 nm)/Co_3O_4 (red trace), and TiO_2 (5 nm)/SiO_2 (2 nm)/Co_3O_4 (12 nm) (blue trace) under condition of (a). Applied potential was 0.096 V vs. RHE. The small dots in the plot are the experimental data and the solid lines represent the results of fitting the data to the Randles circuit.

Independent of specific applications, functional ultrathin oxide nanowalls typically require multi-oxide stacked nanolayers with different chemical properties to have desired catalytic, transport, and chemical separation properties. Therefore, proton conductivity and O_2 impermeability studies were accomplished in multilayer configurations, specifically for Pt/TiO_2 (5 nm)/SiO_2 (2 nm), Pt/SiO_2 (2 nm)/Co_3O_4 (12 nm) and Pt/TiO_2 (5 nm)/SiO_2 (2 nm)/Co_3O_4 (12 nm) electrodes. **Figure 7(a)** and **7(b)** show CV waves under N_2 saturation and O_2 bubbling, respectively, for bare Pt (black trace), Pt/TiO_2 (5 nm)/SiO_2 (2nm) (red trace), Pt/SiO_2 (2 nm)Co_3O_4 (12 nm) (blue trace), and Pt/TiO_2 (5 nm)/SiO_2 (2 nm)/Co_3O_4 (12 nm) (green trace). None of the multilayer constructs exhibit O_2 permeation in agreement with the oxygen blocking property of the 2 nm SiO_2 layer.

For stacked SiO_2 (2 nm)/Co_3O_4 (12 nm) layers, the observed high H^+ flux of 7,700 s^{-1} nm^{-2} obtained by EIS, compared with 2,900 s^{-1} nm^{-2} for bare Co_3O_4 (12 nm), reveals a flux enhancement of 2.6 $\pm$ 0.7 by the added silica layer (**Figure 7(c)** and Table 1). A similarly strong H^+ flux increase is observed in the case of titania. Here, the flux of 2,700 H^+ s^{-1} nm^{-2} for TiO_2 (5 nm)/SiO_2 (2 nm) exceeds 830 s^{-1} nm^{-2} for a single 5 nm TiO_2 layer by a factor of 3.3 $\pm$ 1.4. Therefore, the ALD-grown ultrathin SiO_2 enables fast proton delivery across multi-oxide stacked nanolayers.

As shown by the Nyquist EIS plot in **Figure 7(c)** and data summarized in Table 1, Z_W for triple layers Pt/TiO_2 (5 nm)/SiO_2 (2 nm)/Co_3O_4 (12 nm) is 46 Ω, corresponding to a proton flux of 2,400 s^{-1} nm^{-2}. The result confirms that the H^+ transfer enhancement effect for dual layer Co_3O_4/SiO_2 and TiO_2/SiO_2 samples is preserved in a triple layer construct.

3. Discussion

3.1 Ultrathin Silica Layer Facilitates Proton Transport across Solid-to-Solid Interfaces

Fluid mechanics analysis using the scheme visualized in Figure S3 and Fick's law (1), Einstein relation (2 and 3), expression for uniform electric field (4), and Arrhenius equation (5)[44,52] allow us to characterize the H^+ flux in terms of standard parameters. Under the steady-state operation, relevant parameters and constants are defined as follows: $J(H^+)$ is the proton flux, $D(H^+)$ proton diffusivity, $C(H^+)$ proton concentration, $x(SiO_2)$ silica membrane thickness, $\mu(H^+)$ proton mobility, $V_d(H^+)$ average drift velocity of protons in amorphous silica, E_a activation energy required for proton hopping in amorphous silica, E uniform electric field, k_B Boltzmann constant, T temperature (295 K for the experiments reported here), ΔV applied voltage between working

and counter electrodes (– 1.1 V), d average distance between the two electrodes (2 cm), *R* ideal gas constant, and $D_o(H^+)$ low-limit diffusion constant of SiO_2 estimated to be 0.025 cm^{-2} s^{-1}.[52]

$$J(H^+) = -D(H^+)\frac{\mathrm{dC}(H^+)}{\mathrm{dx}(SiO_2)} \quad (1)$$

$$D(H^+) = \mu(H^+)k_BT \quad (2)$$

$$\mu(H^+) = \frac{V_d(H^+)}{\mathrm{E}} \quad (3)$$

$$E = -\frac{\Delta \mathrm{V}}{\mathrm{d}} \quad (4)$$

$$D(H^+) = D_o(H^+)\exp(\frac{-E_a}{\mathrm{RT}}) \quad (5)$$

The calculated fluid mechanics parameters are summarized in Table 2. According to the analysis, at 295 K, – 1.1 V applied potential, and proton concentration corresponding to pH 4, an activation energy (E_a) around 5 kcal/mol is associated with proton hopping in the amorphous silica membrane. Protons move through the silica membrane at velocity V_d between 830 and 1100 nm s^{-1}, resulting in proton mobility μ of 1.5 x 10^{10} to 2.0 x 10^{10} nm^2 s^{-1} V^{-1} and thus, diffusivity (*D*) ranging from 4.0 x 10^8 to 5.0 x 10^8 nm^2 s^{-1}. The latter is in reasonable agreement with the theoretical value (MD simulation) of 1.7 x 10^8 nm^2 s^{-1} reported for amorphous SiO_2.[53] The mechanism of proton diffusion through amorphous silica is currently understood as proton hopping whereby H^+ transiently binds/dissociates from oxygen atoms throughout the interior of the solid (Grotthuss mechanism).[53-55] These oxygen sites in the silica interior appear as Si-O-Si (siloxane) bridges, SiOH (silanol), and $Si\text{-}O^-$ (siloxy), all of which have been considered as participating in the hopping process.[53,54]

Two factors point to the dominant role of H^+ hopping along bridging oxygens of siloxane moieties. IRRAS data of ALD-grown silica layers show only very small, if any, Si-OH absorptions (Figure 3(c); the region above 3600 cm^{-1} is typical for non-H bonded SiOH, and a

broad band between 3600 and 3000 cm^{-1} for H-bonded Si-OH).[56] Molecular dynamics calculations[53] indicate that H^+ hopping along strained Si-O-Si moieties featuring angles between 125 and 135 degree (unstrained: 150 degree) is competitive with fast H^+ hopping through liquid H_2O; the interior of amorphous SiO_2 has a wide range of Si-O-Si angles from 120 to 180 degree with a substantial density of such strained Si-O-Si bridges in the 125-135 degree range.[53] According to ab initio calculations, activation barriers for H^+ hopping among such strained Si-O-Si bridges could be as low as 5 kcal mol^{-1}.[57] Therefore, we attribute the observed very low barrier for diffusion of H^+ through the silica layer to hopping along O centers of strained siloxane moieties, rather than hopping along Si-OH/Si-O^- sites, which is unlikely in our samples given the absence of a significant concentration of silanol groups, or involvement of protonic defect.[58]

We propose that the proton hopping mechanism along the interfacial oxygen bridges is the origin of the large flux enhancement upon incorporating ultrathin SiO_2 into multi-oxide stacked nanolayers, which is the main discovery of this work. Specifically, the three-fold increase of the H^+ flux when adding a 2 nm silica layer to the Pt/TiO_2 (5 nm) sample is attributed to the formation of Ti-O-Si linkages observed by infrared spectroscopy, replacing the TiO_2/electrolyte interface exhibiting inefficient H^+ transfer with the efficient SiO_2/electrolyte proton transfer interface and an interface featuring Ti-O-Si bridges that enable fast proton hopping from the interface to TiO_2. An analogous H^+ hopping pathway, opened up by the spectroscopically observed Co-O-Si bridges, capacitates the 2.6-fold increase of the proton flux. It is further aided by improvement of the H^+ reduction kinetics by the replacement of the Pt/Co_3O_4 interface (R_{CT} 7.0 Ω) by the Pt/SiO_2 interface (R_{CT} 2.1 Ω). We conclude that few

nanometer thick amorphous silica layers substantially boost H^+ transfer across contiguous oxide layers.

3.2 Proton Transport and Chemical Separation Properties fit Requirements for Oxide Nanowalls of Artificial Photosystems

The observed O_2 permeability of the ALD-grown Co_3O_4 nanolayers (Figure 5(b)) is consistent with their nanogranular nature of the layers (uniform films of 3-5 nm particles),[22] providing grain boundary networks that offers diffusion paths for O_2 as well as proton across the entire film. This obviates the need for H^+ hopping through the interior of Co_3O_4 crystals. Rather, a plausible mechanism is diffusion of H^+ along the grain boundary surfaces in the interior of the polycrystalline layer as previously found for proton transport across thin films of polycrystalline ceria or yttria-stabilized zirconia at low temperature.[59-63] The conductivity κ of ALD-grown nanogranular Co_3O_4 ALD layers of 3.8×10^{-8} S cm^{-1} (pH 4) is close to previously reported room temperature values of 2×10^{-8} S cm^{-1} for nanograin-sized yttria-stabilized zirconia layers.[60] The close values for these nanogranular layers having different chemical composition supports diffusion through grain boundaries since this mechanism is independent of the chemical nature of the nanoparticle interior.

In the case of ALD-grown TiO_2 layers, infrared evidence indicates polycrystalline anatase structure. In contrast to Co_3O_4 nanolayers, the titania layer blocks permeation of O_2 for thicknesses exceeding 2 nm (Figure 6(b)), implying that grain boundaries are not accessible for beyond 2 nm. We speculate that H^+ transport through the TiO_2 layers occurs by hopping along TiO_2 particle boundaries, with pathways diminishing beyond 2 nm. However, we cannot rule out the presence of a small percentage of amorphous TiO_2 filling the spaces between grain

boundaries because the signal-to-noise for detecting the corresponding infrared signal, a very broad band in the 600-700 cm^{-1} region,[38] may be inadequate. This leaves open the possibility of Grotthuss type H^+ hopping through the amorphous phase between grain boundaries, like the proposed mechanism for other group IVB metal oxides such as Zr.[64,65] For layers thicker than 2 nm, this hopping path might become too long or no longer contiguous across the full depth of the layer, consistent with the observation that O_2 transmission ceases for greater than 2 nm thickness as well.

The proton conductivity and oxygen permeability resulting from individual and the stacked ultrathin oxide layers perfectly fit the requirements for complete nanoscale artificial photosystems with built-in separation membrane.[16,17] Our specific systems design for vapor phase CO_2 photoreduction by H_2O under membrane separation on the nanoscale consists of a square inch-sized array of Co_3O_4 (12 nm)/SiO_2 (2 nm) core-shell nanotubes as shown in Figure S4. At the current stage of developing the nanotube array, an additional 5 nm TiO_2 layer is deposited on the outside of each nanotube to maintain structural stability. For O_2 permeability, all layers show the desired properties. Specifically, ALD-grown 2 nm silica layers completely block O_2, thus preventing oxygen crossover from the Co oxide layer for water oxidation to the TiO_2 layer with deposited Cu nanocatalysts for CO_2 reduction. At the same time, Co oxide layers of all thicknesses examined are permeable to O_2, assuring the access of H_2O and O_2 molecules to the interior of the polycrystalline Co oxide film for catalytic transformation of H_2O to O_2, thereby substantially enhancing the water oxidation rate per geometrical nanotube wall area. The enhancement of interfacial H^+ transfer by inserting the SiO_2 nanolayer into multilayer nanowalls affords proton flux values of several thousand s^{-1} nm^{-2}, thereby readily exceeding the proton flux

across the nanotube wall to keep up with the photon flux under maximum solar intensity (1,500 photons s^{-1} nm^{-2}).[66]

For maximum solar flux, the required proton flux from the inside of a core-shell nanotube to the outside can be estimated based on the tube geometry. At present, $Co_3O_4/SiO_2/TiO_2$ core-shell nanotubes fabricated in our lab feature 500 nm diameter and 5 μm length, with wall thickness of less than 20 nm.[16] Taking the square area of 2.5 x 10^5 nm^2 defined by the tube diameter as the footprint of the tube exposed to the sun, 3.75 x 10^8 photons s^{-1} nm^{-2} illuminate the nanotube. Therefore, the upper limit for the number of protons produced on the inside of the nanotube is 3.75 x 10^8 H^+ s^{-1} (single photon light absorber). With a nanotube wall surface of 7.85 x 10^6 nm^2, a resulting required radial H^+ flux of 48 H^+ s^{-1} nm^{-2} is calculated. This estimate constitutes an upper limit for the required proton flux from the inside of each tube across the wall to the outside: In the case of 1-photon light absorbers, a large fraction of solar photons is not absorbed, while for a 2-photon tandem light absorption system only half of the incident solar photons (maximum 750 photons s^{-1} nm^{-2}) generate protons. The finding that ALD grown Co_3O_4 layers between 3.5 and 12 nm, SiO_2 layers between 2 and 6 nm, and stacked Co_3O_4 (12 nm)/SiO_2 (2 nm)/TiO_2 (5 nm) layers transmit protons at fluxes exceeding 1,500 s^{-1} nm^{-2} shows that all layers have capacity for accommodating proton flux far beyond the solar flux requirement. We conclude that ultrathin Co_3O_4, SiO_2, TiO_2, and their stacks transport protons at fluxes by far in excess of what is required for use in nanoscale artificial photosystems of any morphology, and for systems with core-shell nanotube geometry in particular, while providing complete chemical separation of the incompatible catalytic environments.

4. Conclusions

Quantitative evaluation by EIS of the proton conductivity of ultrathin multi-oxide layers has revealed that incorporation of 2 nm ALD-grown silica layer substantially boosts proton mass transport across the whole stack. Interfacial covalent oxygen linkages among stacked ALD-grown oxide layers detected by FT-IRRAS are proposed to be the mechanistic origin of enhanced H^+ transfer across the oxide interfaces by providing proton hopping pathways. At the same time, the ultrathin silica layer completely blocks crossover of oxygen (and other small molecules). These findings enable integration of incompatible catalytic functions on the nanoscale, thereby opening up an enormous design space for developing macroscale systems by taking advantage of the virtually unlimited possibilities of diverse nanostructures. The core-shell nanotube array geometry for developing an artificial photosystem with the goal of separating CO_2 reduction and H_2O oxidation environments on all length scales from nano to macro is just one among many opportunities to pursue.

5. Experimental Section

Pt electrode Fabrication: 2 nm Ti adhesive layer and 100 nm of Pt (99.99%) were consecutively deposited by e-Beam evaporation (Semicore SC600 e-beam evaporator) at $< 2 \times 10^{-6}$ Torr on Si wafers (prime grade p-type, Addison Engineering Inc.) precleaned by standard RCA procedure.

Co_3O_4 Atomic Layer Deposition: Atomic Layer Deposition (ALD) of cobalt oxide was carried out using an Oxford FlexAl-Plasma Enhanced ALD system situated in a Class 1000 cleanroom. The process temperature is 40 °C, and bis-(cyclopentadienyl)cobalt(II) (cobaltocene, $CoCp_2$; min

98% from STREM Chemicals, Inc.) is used as a precursor, heated to 80 °C and bubbled with 200 sccm high purity Ar during pulse. Oxygen flow and chamber pressure were maintained at 60 sccm and 15 mTorr during the deposition process. $CoCp_2$ dose was 5 s long, followed by 5 s of purging. Oxygen plasma half-cycle was 1 s pre-plasma, 5 s plasma (300 W) and 15 s purging. Fifty-four such cycles lead to a deposition of 3.5 $\pm$ 0.8 nm thick Co_3O_4 layer.

SiO_2 Atomic Layer Deposition: ALD of silicon dioxide was conducted with the same Oxford FlexAl-Plasma Enhanced ALD system. The process temperature is 40 °C, and tris(dimethylamino)silane (3DMAS; min 99% from STREM Chemicals, Inc.) and oxygen plasma served as a precursor and the oxidant, respectively. Oxygen gas flow was held at 60 sccm throughout the deposition process. The silicon precursor exposure half cycle consisted of 2 s dosing and 10 s purging using 250 sccm high purity Ar gas. The oxygen plasma half cycle consisted of 2 s pre-plasma treatment, 3 s plasma exposure, and 5 s purging with 100 sccm N_2 and 250 sccm Ar. The plasma power was 250 W and was applied for 3 s during the oxygen plasma half cycle. The deposition chamber pressure was held at 80 mTorr during the 3DMAS dosing and purging steps and 15 mTorr during the oxygen plasma steps. Twenty such cycles lead to a deposition of 2.0 $\pm$ 0.6 nm thick SiO_2 layer.

TiO_2 Atomic Layer Deposition: ALD of titanium dioxide was conducted with the same Oxford FlexAl-Plasma Enhanced ALD system. The process temperature is 40 °C, and tetrakis(dimethylamido)titanium(IV) (TDMAT; 99.999% from Sigma Aldrich) and oxygen plasma served as a precursor and an oxidant, respectively. Oxygen gas flow was kept at 60 sccm throughout the deposition process. The titanium precursor exposure half cycle consisted of 2 s

dosing and 10 s purging using 250 sccm high purity Ar gas. The oxygen plasma half cycle consisted of 2 s pre-plasma treatment, 3 s plasma exposure, and 5 s purging with 100 sccm N_2 and 250 sccm Ar. Plasma power of 250 W was applied for 3 s during the oxygen plasma half cycle. The deposition chamber pressure was held at 80 mTorr during the TDMAT dosing and purging steps and 15 mTorr during the oxygen plasma steps. Forty-five such cycles lead to a deposition of 5.0 $\pm$ 0.07 nm thick TiO_2 layer.

Electrode Preparation: To make an ohmic contact on each electrode sample and expose only its target surface area of interest to electrolyte, silver paste and epoxy resin were used as in previous studies.[67,68] First, each sample was gently scratched to expose about 2×2 mm^2 area of Pt. Then copper wire was attached on the exposed Pt surface by applying conductive silver paint (Electron Microscopy Sciences) to the wire/Pt interface. The paint was left to dry (hardening) at ambient conditions for one hour. The electrical connection, sample edges and rear side were covered with epoxy resin (Hysol 615; Loctite) and hardened overnight.

Electrochemical Characterization: Cyclic Voltammetry (CV) and Electrochemical Impedance Spectroscopy (EIS) measurements were accomplished using a CH Instruments model CHI604E potentiostat in the standard three-electrode configuration, containing with a Ag/AgCl in 3 M KCl (BASi RE5B) as the reference electrode, a Pt wire as the counter electrode, and ALD-grown oxide(s) on Pt electrode as the working electrode (WE). The aqueous electrolyte solution consisted of 0.5 M sodium sulfate (99.0%, Sigma-Aldrich) and the solution pH was adjusted to 4 using sulfuric acid (95–98%, Sigma-Aldrich). The solution was purged with high purity nitrogen gas (Grade 5.0, Praxair) for 20 minutes before CV measurements, or continuously bubbled with

oxygen gas (Grade 4.3, Praxair) during the measurements. All reagents were used as-received without further purification.

Prior to all CV measurements at scan rate of 50 mV s^{-1} under N_2 saturation or O_2 bubbling, 5 dummy cycles were first performed using the same parameters in order to stabilize the electrode sample and remove any adventitious impurities.[22,24,67,68] After obtaining J-V plots of CV measurements, EIS Nyquist plots were obtained at -0.36 V vs. Ag/AgCl (0.096 V vs. RHE) applied voltage using a small amplitude of 5 mV in the frequency range 1 – 10^5 Hz.[44] The applied potential on the WE with respect to the Pt wire counter electrode, which is needed for calculating the current density (proton flux) from the measured resistivity, was determined as -1.1 V by recording of an auxiliary signal under N_2 saturation.

EIS Data Analysis: The resulting EIS data were analyzed by using the software Z-view.[49] The program enables the detailed analysis by equivalent circuit fitting routines of the raw impedance data, which affords interpretation of cell parameters (diffusion rate, series resistance, polarization resistance).

Thickness Measurements: The thicknesses of atomic layer deposited oxide thin films were measured using spectroscopic ellipsometry (Horiba Jobin UVISEL) in the 900-250 nm range at angles varying from 45 to 70° with 5° steps.

FT-IRRAS: Polarized FT-IRRAS spectra (Fourier transform infrared reflection absorption spectroscopy) of samples Pt/SiO_2, Pt/Co_3O_4, Pt/Co_3O_4/SiO_2, and Pt/TiO_2/SiO_2/Co_3O_4 were recorded on a Bruker FT-IR spectrometer model Vertex 80 equipped with LN_2 cooled HgCdTe

detectors Kolmar model KMPV11-1-J2 with a 14 μm bandgap or Infrared Associates model D315 with a 25 μm bandgap, computer controlled reflection accessory Bruker model A513/QA, and wire-grid polarizer model F350. The mirror angle of the IRRAS accessory was fixed at 78° and the grid polarizer switched between p and s polarization. Using an aperture of 2.5 mm, twenty spectra of 400 scans at 2 cm^{-1} resolution were recorded and averaged. For analysis, sample single beam spectra with p polarization were divided by single beam spectra of reference sample (aluminum mirror) and the negative logarithm taken. A corresponding absorbance spectrum for the s polarized configuration was computed and subtracted from the p polarized absorbance spectrum.[69,70]

$$-\log_{10}(\text{p, sample/p, ref}) - [-\log_{10}(\text{s, sample/s, ref})]$$

From this result, a background was subtracted which is specified for each spectrum shown in Sect. 3. The latter was determined by the same computational method as used for the sample. All figures show spectra calculated according to this method, unless noted otherwise. Bands of residual atmospheric water vapor in the sample compartment were computationally eliminated as well. For measurements of the Pt-H and Pt-D bands after electrochemical runs, samples were kept in O_2-free atmosphere (N_2 or Ar) throughout electrochemical runs, transfer to and handling in the IRRAS sample compartment.

AFM: AFM (Atomic Force Microscopy) was carried out using a Bruker Dimension Icon operated with a Tap150Al-G probe in tapping mode. Surface roughness data were obtained and images were corrected with a freeware, Gwyddion. The surface roughness of Pt films covered by ultrathin ALD-grown layers of TiO_2, SiO_2, and Co_3O_4 are shown in Figure S5.

Supporting Information

Supporting Information is available from the Wiley Online Library.

Acknowledgment

Funding to support this work was provided by the Energy & Biosciences Institute through the EBI-Shell program. Portions of this work (plasma enhanced atomic layer deposition, ellipsometry, e-beam evaporation) were performed as a User Project at The Molecular Foundry, Lawrence Berkeley National Laboratory, which is supported by the Office of Science, Office of Basic Energy Sciences, of the U.S. Department of Energy under Contract No. DE-AC02-05CH11231. We thank Prof. Daniel Esposito, Columbia University, as well as Mr. Lin Su and Prof. Caroline Ajo-Franklin, Rice University, for insightful discussions of electrochemical measurements.

Conflict of Interest

The authors declare no conflict of interest.

References

[1] Y. W. Chen, J. D. Prange, S. Duehnen, Y. Park, M. Gunji, C. E. D. Chidsey, P. C. McIntyre, *Nature Mater.* **2011**, *10*, 539.

[2] A. G. Scheuermann, J. P. Lawrence, K. W. Kemp, T. Ito, A. Walsh, C. E. D. Chidsey, P. K. Hurley, P. C. McIntyre, *Nature Mater.* **2016**, *15*, 99.

[3] S. Hu, M. R. Shaner, J. A. Beardslee, M. Lichterman, B. S. Brunschwig, N. S. Lewis, *Science* **2014**, *344*, 1005.

[4] E. Verlage, S. Hu, R. Liu, R. J. R. Jones, K. Sun, C. Xiang, N. S. Lewis, H. A. Atwater, *Energy Environ. Sci.* **2015**, *8*, 3166.

[5] K. Maeda, K. Teramura, S. Lu, N. Saito, Y. Inoue, K. Domen, *Angew. Chem. Int. Ed.* **2006**, *45*, 7806.

[6] T. Hisatomi, K. Domen, *Curr. Opin. Electrochem.* **2017**, *2*, 148.

[7] N. Y. Labrador, E. L. Songcuan, C. De Silva, H. Chen, S. J. Kurdziel, R. K. Ramachandran, C. Detavernier, D. V. Esposito, *ACS Catal.* **2018**, *8*, 1767.

[8] D. V. Esposito, *ACS Catal.* **2018**, *8*, 457.

[9] H. Husin, W. N. Su, C. J. Pan, J. Y. Liu, J. Rick, S. C. Yang, W. T. Chuang, H. S. Sheu, B. J. Hwang, *Int. J. Hydrogen Energy* **2013**, *38*, 13529.

[10] J. Y. Lee, J. G. Lee, S. H. Lee, M. Seo, L. Piao, J. H. Bae, S. Y. Lim, Y. J. Park, T. D. Chung, *Nature Commun.* **2013**, *4*:2766.

[11] C. W. Moore, J. Li, P. A. Kohl, *J. Electrochem. Soc.* **2005**, *152*, A1606.

[12] Y. Aoki, E. Muto, A. Nakao, T. Kunitake, *Adv. Mater.* **2008**, *20*, 4387.

[13] F. A. L. Laskowski, M. R. Nellist, J. Qui, S. W. Boettcher, *J. Am. Chem. Soc.* **2019**, *141*, 1394.

[14] R. J. Kamire, M. B. Majewski, W. L. Hoffeditz, B. T. Phelan, O. K. Farha, J. T. Hupp, M. R. Wasielewski, *Chem. Sci.* **2017**, *8*, 541.

[15] M. K. Brennaman, R. J. Dillon, L. Alibabaei, M. K. Gish, C. J. Dares, D. L. Ashford, R. L. House, G. J. Meyer, J. M. Papanikolas, T. J. Meyer, *J. Am. Chem. Soc.* **2016**, *138*, 13085.

[16] E. Edri, S. Aloni, H. Frei, *ACS Nano* **2018**, *12*, 533.

[17] W. Kim, E. Edri, H. Frei, *Acc. Chem. Res.* **2016**, *49*, 1634.

[18] J. A. Cornejo, H. Sheng, E. Edri, C. M. Ajo-Franklin, H. Frei, *Nature Commun.* **2018**, *9*:2263.

[19] G. Katsoukis, H. Frei, *ACS Appl. Mater. Interfaces* **2018**, *10*, 31422.

[20] H. S. Soo, A Agiral, A. Bachmeier, H. Frei, *J. Am. Chem. Soc.* **2012**, *134*, 17104.

[21] A. Agiral, H. S. Soo, H. Frei, *Chem. Mater.* **2013**, *25*, 2264.

[22] E. Edri, H. Frei, *J. Phys. Chem. C* **2015**, *119*, 28326.

[23] E. Edri, J. K. Cooper, I. D. Sharp, D. M. Guldi, H. Frei, *J. Am. Chem. Soc.* **2017**, *139*, 5458.

[24] G. Yuan, A. Agiral, N. Pellet, W. Kim, H. Frei, *Faraday Discuss.* **2014**, *176*, 233.

[25] M. Yoshida, K. Takanabe, K. Maeda, A. Ishikawa, J. Kubota, Y. Sakata, Y. Ikezawa, K. Domen, *J. Phys. Chem. C* **2009**, *113*, 10151.

[26] R. M. Almeida, C. G. Pantano, *J. Appl. Phys.* **1990**, *68*, 4225.

[27] L. F. Pena, C. E. Nanayakkara, A. Mallikarjunan, H. Chandra, M. Xiao, X. Lei, R. M. Pearlstein, A. Derecskei-Kovacs, Y. J. Chabal, *J. Phys. Chem. C* **2016**, *120*, 10927.

[28] B. B. Burton, S. W. Kang, S. W. Rhee, S. M. George, *J. Phys. Chem. C* **2009**, *113*, 8249.

[29] R. Tian, O. Seitz, M. Li, W. Hu, Y. J. Chabal, *Langmuir* **2010**, *26*, 4563.

[30] C. T. Kirk, *Phys. Rev. B* **1988**, *38*, 1255.

[31] J. Wang, B. Zou, M. A. El-Sayed, *J. Mol. Struct.* **1999**, *508*, 87.

[32] Y. Li, W. Qui, F. Qin, H. Fang, V. G. Hadjiev, D. Litvinov, J. Bao, *J. Phys. Chem. C* **2016**, *120*, 4511.

[33] Q. Guo, X. Guo, Q. Tian, *Adv. Powder Tech.* **2010**, *21*, 529.

[34] J. F. Huang, A. Hung, C. B. Wang, C. T. Yeh, *J. Chin. Chem. Soc.* **2002**, *49*, 819.

[35] K. B. Klepper, O. Nilsen, H. Fjellvag, *Thin Solid Films* **2007**, *515*, 7772.

[36] S. Portal, R. M. Almeida, *Phys. Stat. Sol. (a)* **2004**, *201*, 2941.

[37] T. Busani, R. A. B. Devine, *Semicond. Sci. Technol.* **2005**, *20*, 870.

[38] C. Pecharroman, F. Gracia, J. P. Holgado, M. Ocana, A. R. Gonzalez-Elipe, J. Bassas, J. Santiso, A. Figueras, *J. Appl. Phys.* **2003**, *93*, 4634.

[39] G. Katsoukis, W. J. Jo, H. Frei, *J. Phys. Chem. C* **2019**, *123*, 18905.

[40] R. M. Almeida, A. C. Marques, S. Pelli, G. C. Righini, A. Chiasera, M. Mattarelli, M. Montagna, C. Tosello, R. R. Goncalves, H. Portales, S. Chaussedent, M. Ferrari, L. Zampedri, *Phil. Mag.* **2004**, *84*, 1659.

[41] R. J. Nichols, A. Bewick, *J. Electroanal. Chem.* **1988**, *243*, 445.

[42] H. Ogasawara, M. Ito, *Chem. Phys. Lett.* **1994**, *221*, 213.

[43] T. Shinagawa, K. Takanabe, *Phys. Chem. Chem. Phys.* **2015**, *17*, 15111.

[44] A. J. Bard, L. R. Faulkner, *Electrochemical Methods*, 2nd ed., Wiley, New York **2001**.

[45] M. E. S. Beatty, H. Chen, N. Y. Labrador, B. J. Lee, D. V. Esposito, *J. Mater. Chem. A* **2018**, *6*, 22287.

[46] W. J. Jo, J. W. Jang, K. J. Kong, H. J. Kang, J. Y. Kim, H. Jun, K. P. S. Parmar, J. S. Lee, *Angew. Chem. Int. Ed.* **2012**, *124*, 3201.

[47] A. T. Heijne, O. Schaezle, S. Gimenez, F. Fabregat-Santiago, J. Bisquert, D. P. B. Strik, F. Barrière, C. J. N. Buisman, H. V. M. Hamelers, *Energy Environ. Sci.* **2011**, *4*, 5035.

[48] V. Freger, S. Bason, *J. Membr. Sci.* **2007**, *302*, 1.

[49] https://www.ameteksi.com/products/software/zview-software

[50] S. Prakash, W. E. Mustain, S. H. Park, P. A. Kohl, *J. Power Sources* **2008**, *175*, 91.

[51] M. Nogami, K. Miyamura, Y. Abe, *J. Electrochem. Soc.* **1997**, *144*, 2175.

[52] J. D. McBrayer, R. M. Swanson, T. W. Sigmon, *J. Electrochem. Soc.* **1986**, *133*, 1242.

[53] J. C. Fogarty, H. M. Aktulga, A. Y. Grama, A. C. T. van Duin, S. A. Pandit, *J. Chem. Phys.* **2010**, *132*, 174704.

[54] G. Lockwood, S. H. Garofalini, *J. Chem. Phys.* **2009**, *131*, 074703.

[55] H. Cesiulis, N. Tsyntsaru, A. Ramanavicius, G. Ragoisha, *Nanostructures and Thin Films for Multifunctional Applications,* Springer, New York **2016**.

[56] C. Wang, M. Nogami, Y. Abe, *J. Sol-Gel Sci. & Technol.* **1999**, *14*, 273.

[57] H. A. Kurtz, S. P. Karna, *IEEE Trans. Nucl. Sci.* **1999**, *46*, 1574.

[58] K. D. Kreuer, *Chem. Mater.* **1996**, *8*, 610.

[59] T. S. Oh, D. A. Boyd, D. G. Goodwin, S. M. Haile, *Phys. Chem. Chem. Phys.* **2013**, *15*, 2466.

[60] H. J. Avila-Paredes, C. T. Chen, S. Wang, R. A. De Souza, M. Martin, Z. Munir, S. Kim, *J. Mater. Chem.* **2010**, *20*, 10110.

[61] S. Kim, H. J. Avila-Paredes, S. Wang, C. T. Chen, R. A. De Souza, M. Martin, Z. A. Muir, *Phys. Chem. Chem. Phys.* **2009**, *11*, 3035.

[62] M. Shirpour, G. Gregori, R. Merkle, J. Maier, *Phys. Chem. Chem. Phys.* **2011**, *13*, 937.

[63] M. Nakamura, T. Aoki, Y. Hatanaka, D. Korzec, J. Engemann, *J. Mater. Res.* **2001**, *16*, 621.

[64] E. C. C. De Souza, R. Muccillo, *Mater. Res.* **2010**, *13*, 385.

[65] Z. Tao, L. Yan, J. Qiao, B. Wang, L. Zhang, J. Zhang, *Prog. Mater. Sci.* **2015**, *74*, 1.

[66] Solar Spectra, National Renewable Energy Laboratory, Golden, CO, USA. http://rredc.nrel.gov/solar/spectra/am1.5

[67] W. J. Jo, J. T. Nelson, S. Chang, V. Bulović, S. Gradečak, M. S. Strano, K. K. Gleason, *Adv. Mater.* **2016**, *28*, 6399.

[68] W. J. Jo, D. C. Borrelli, V. Bulović, K. K. Gleason, *Org. Electron.* **2015**, *26*, 55.

[69] Hollins, P. *Infrared Reflection-Absorption Spectroscopy, Encyclopedia of Analytical Chemistry*, Wiley, New York **2006**.

[70] Y. J. Chabal, *Surf. Sci. Rep.* **1988**, *8*, 211.

Table 1. Electrochemical parameters gained by EIS data analysis

Materials coated on Pt electrode	Potential [V]	R_{CT}: Charge-transfer resistance [Ω]	Z_W: Warburg impedence [Ω]	Surface [cm^2]	Thickness [nm]	J: Current densitiy [A cm^{-2}]	H^+ flux [s^{-1} nm^{-2}]
SiO_2 [2 nm]	-1.1	2.5 ± 0.3	6.8 ± 1.6	0.68 ± 0.05	2 ± 0.6	-0.24 ± 0.07	15000 ± 4600
SiO_2 [4 nm]	-1.1	4.9 ± 0.3	17.5 ± 1.2	0.68 ± 0.005	4 ± 0.03	-0.092 ± 0.007	5800 ± 440
SiO_2 [6 nm]	-1.1	36.8 ± 0.5	34.1 ± 3.2	0.525 ± 0.01	6 ± 0.1	-0.062 ± 0.007	3800 ± 430
Co_3O_4 [3.5 nm]	-1.1	2.9 ± 0.2	19.9 ± 0.8	0.35 ± 0.003	3.5 ± 0.8	-0.160 ± 0.008	9900 ± 490
Co_3O_4 [7 nm]	-1.1	3.0 ± 0.2	22.9 ± 1.0	0.56 ± 0.015	7 ± 0.1	-0.086 ± 0.006	5400 ± 380
Co_3O_4 [12 nm]	-1.1	7.0 ± 0.3	37.1 ± 1.7	0.64 ± 0.007	12 ± 0.04	-0.047 ± 0.003	2900 ± 170
TiO_2 [2 nm]	-1.1	17.0 ± 0.9	156.6 ± 5.6	0.28 ± 0.04	2 ± 0.02	-0.026 ± 0.005	1600 ± 280
TiO_2 [5 nm]	-1.1	194.5 ± 2.9	305.3 ± 12.5	0.27 ± 0.09	5 ± 0.07	-0.013 ± 0.005	830 ± 310
TiO_2 [10 nm]	-1.1	N/A	5594 ± 300	0.56 ± 0.01	10 ± 0.05	-0.00035 ± 0.00003	22 ± 2
SiO2 [2 nm]/Co3O4 [12 nm]	-1.1	2.1 ± 0.8	9.7 ± 2.6	0.92 ± 0.09	14 ± 0.6	-0.12 ± 0.03	7700 ± 2000
TiO_2 [5 nm]/SiO_2 [2 nm]	-1.1	3.8 ± 3.2	43 ± 9	0.6 ± 0.08	7 ± 0.6	-0.043 ± 0.009	2700 ± 540
TiO_2 [5 nm]/SiO_2 [2 nm]/Co_3O_4 [12 nm]	-1.1	4.2 ± 0.2	46 ± 1.2	0.63 ± 0.02	19 ± 0.7	-0.038 ± 0.001	2400 ± 60

a) Thickness is determined by ellipsometry. Surface roughness in the form of AFM images is shown in Figure S5.

Table 2. Proton diffusion parameters of silica membrane obtained by Fluid mechanics

Thickness [nm]	H^+ flux [s^{-1} nm^{-2}]	$dC(H^+)/dx$ [s^{-1} nm^{-4}]	$D(H^+)$ [nm^2 s^{-1}]	$\mu(H^+)$ [nm^2 s^{-1} V^{-1}]	V_d (H^+) [nm s^{-1}]	E_a [kcal mol^{-1}]
2	1.50E+04	3.01E-05	4.97E+08	1.95E+10	1.07E+03	4.99645736
4	5.77E+03	1.51E-05	3.83E+08	1.51E+10	8.29E+02	5.148580913
6	3.83E+03	1.00E-05	3.82E+08	1.50E+10	8.27E+02	5.150302478

Table of Contents Graphics

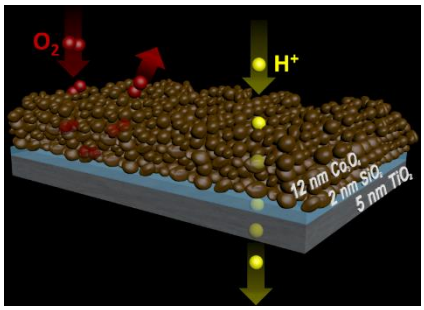

Ultrathin amorphous silica sandwiched between metal oxide nanolayers substantially enhances proton transfer across the multi-oxide stack while blocking crossover of oxygen molecules. The boosting effect is attributed to proton hopping pathways enabled by covalent oxygen bridges across the solid-solid interfaces. The finding enables the integration of incompatible catalytic functions on the nanoscale, opening up an enormous design space for scaling up to macro-sized systems.